Halide-based solid-state electrolyte as an interfacial modifier for high performance solid-state Li–O$_2$ batteries

Changtai Zhao [a], Jianwen Liang [a], Xiaona Li [a], Nathaniel Holmes [a], Changhong Wang [a], Jian Wang [b], Feipeng Zhao [a], Shaofeng Li [e], Qian Sun [a], Xiaofei Yang [a], Jianneng Liang [a], Xiaoting Lin [a], Weihan Li [a], Ruying Li [a], Shangqian Zhao [c], Huan Huang [d], Li Zhang [c], Shigang Lu [c], Xueliang Sun [a],*

[a] *Department of Mechanical and Materials Engineering, University of Western Ontario, London, ON, N6A 5B9, Canada*
[b] *Canadian Light Source Inc., University of Saskatchewan, 44 Innovation Boulevard, Saskatoon, SK, S7N 2V3, Canada*
[c] *China Automotive Battery Research Institute Co., Ltd., Beijing, 100088, PR China*
[d] *Glabat Solid-State Battery Inc., 700 Collip Circle, London, ON, N6G 4X8, Canada*
[e] *Stanford Synchrotron Radiation Lightsource, SLAC National Accelerator Laboratory, Menlo Park, CA, 94025, USA*

A R T I C L E   I N F O

A B S T R A C T

Solid-state electrolyte and solid-state air electrode design are the main bottlenecks inhibiting the development of solid-state Li–O$_2$ batteries (SSLOBs). Herein, we report an ionically superconductive halide electrolyte which regulates the air electrode interface and enhances the performance of SSLOBs. As this is the first investigation of this halide electrolyte in a Li-O$_2$ battery, a comprehensive study of the stability of this electrolyte is conducted. The high ionic conductivity of Li$_3$InCl$_6$ (up to 1.3×10^{-3} S cm^{-1}) and its solution-based preparation method enable it to work like a liquid electrolyte modifier at the air electrode, uniformly regulating the function of the interface. As a result, Li–O$_2$ batteries with Li$_3$InCl$_6$ exhibit decreased interfacial resistance and enhanced decomposition of discharge products. The present study may open a new window of opportunity toward the development of SSLOBs.

1. Introduction

Solid-state lithium batteries (SSLBs) with solid-state electrolytes (SSEs) have attracted worldwide research interest due to their high theoretical energy density and improved safety [1–4]. Among them, solid-state Li–O$_2$ batteries (SSLOBs) feature the highest theoretical energy density and have been extensively investigated. Some progress has been made in recent years [5–9], however the development of SSLOBs is still plagued by a lack of suitable SSEs and the challenge of designing a solid-state air electrode (SSAE) [10–13].

Despite the progress made in SSE research for applications in solid-state Li-ion batteries [14], we still lack a suitable SSE for SSLOBs due to the unique requirements imposed by a SSLOB's configuration. A SSE for a SSLOB must exhibit good air stability, have a wide electrochemical window (over 4.5 V), make intimate interfacial contact, and must have excellent chemical stability in the presence of the chemical species produced in the electrochemical reaction [15–18]. Sulfide-based SSEs

feature ultra-high ionic conductivity ($>10^{-2}$ S cm^{-1}) and are very malleable, but their poor air stability severely inhibits their feasibility in SSLOBs [19,20]. Polymer-based SSEs have the advantages of low cost and ease of processing, but their low ionic conductivity at room temperature, narrow electrochemical stability window, and poor chemical stability toward discharge products inhibit their application in SSLOBs [21–25]. Oxide-based SSEs may be the most promising SSEs for SSLOBs because of their wide electrochemical stability window, good chemical stability, and excellent mechanical strength [26–29]. Oxide-based SSEs are also attractive for their ability to suppress the growth of Li dendrites and eliminate consequent short circuits [30–32]. However, their relatively low ionic conductivity and large interfacial resistance usually result in severe polarization of batteries, rendering the air electrode design more challenging [14,33].

New SSAEs will also be required in the development of advanced SSLOBs. SSAE design remains exceedingly challenging due to the requirements that the electrode is porous and exhibits good ionic and

* Corresponding author.
  E-mail address: xsun9@uwo.ca (X. Sun).

electronic conductivity [34,35]. The typical SSAE has many solid-state interfaces, including the interface between the discharge products and the ionic conductor, as well as the interface between the discharge products and the electronic conductor [1,36,37]. The ionic conductor and electronic conductor also need to have firm contact for electron/ion exchange and to assist with the formation and decomposition of discharge products. The requirement of a porous structure only complicates the design task. Ultimately, designs for both a suitable SSAE and SSE are required to develop advanced SSLOBs.

Halide-based SSEs have recently attracted researchers' attention due to a breakthrough in ionic conductivity ($>10^{-3}$ S cm^{-1}) and a proposed simpler preparation process [38,39]. To illustrate, Li_3InCl_6 has been reported to have an ionic conductivity as high as 2×10^{-3} S cm^{-1} [40]. It is stable toward oxygen and has a wide electrochemical stability window. More importantly, it can be prepared in an aqueous solution [41]. Li_3InCl_6 therefore has the potential to successfully regulate the air electrode interface and enhance the performance of SSLOBs.

Herein, we show the ability of a halide electrolyte in a SSLOB to optimize the air electrode interface and enhance battery performance. The Li_3InCl_6 electrolyte features an ionic conductivity as high as 1.3×10^{-3} S cm^{-1}, and is stable with both the intermediate products and final products in Li–O_2 batteries. The solution-based preparation method allows for Li_3InCl_6 to be uniformly distributed within the electrode and maintain intimate contact with nitrogen-doped carbon nanotubes (NCNTs) and $Li_{1.5}Al_{0.5}Ge_{1.5}(PO_4)_3$ (LAGP). When this superionic conductor was employed as an interfacial modifier in SSLOBs, interfacial resistance decreased significantly from 2056 Ω to 569 Ω due to the optimized ionic transport channels of the electrode. This resistance is comparable to batteries with liquid electrolytes (LE). The superionic conductor as a modifier also promotes the decomposition of discharge products, improving Coulombic efficiency, and prolonging cycle life. This is confirmed through scanning transmission X-ray microscopy (STXM) results.

2. Experimental section

Preparation of the LAGP-NCNT-Li_3InCl_6 air electrode: LAGP pellets were made by pressing and sintering. LAGP powders were mixed and ground with polyvinyl butyral (PVA) as the binder before being pressed into pellets at 250 MPa. The pellets were then sintered at 960 °C for 6 h. The gel polymer electrolyte (GPE) was prepared with a solution casting method. The solution of poly(vinylidene fluoride-co-hexauoropropylene) (PVDF-HFP) polymer (Mw: 400000), tetraethylene glycol dimethyl ether (TEGDME) solvent, and LiClO$_4$ salt dissolved in acetone was prepared by vigorously stirring overnight. The solution was then cast in a glass dish and dried at room temperature for three days to remove acetone solvent, yielding the GPE. The LAGP and NCNT composite air electrode (LAGP-NCNT) was prepared by dropping the dispersed solution of NCNT and LAGP powders in ethanol on the surface of a LAGP pellet and then sintering at 700 °C for 10 min in Ar atmosphere. The mass ratio of NCNT to LAGP powder is 1 to 5. The LAGP-NCNT modified with Li_3InCl_6 (LAGP-NCNT-Li_3InCl_6) air electrode was prepared by dropping the mixed aqueous solution with LiCl and InCl$_3$ into the LAGP-NCNT air electrode and drying in a vacuum oven at 150 °C overnight. LAGP-NCNT-Li_3InCl_6 air electrodes with different amounts of Li_3InCl_6 were prepared by controlling the amount of solution used. Based on the mass ratio of Li_3InCl_6 to NCNT, the samples were labeled as LAGP-NCNT-0.5Li_3InCl_6, LAGP-NCNT-1Li_3InCl_6, and LAGP-NCNT-2Li_3InCl_6.

Materials Characterization: The SSE and air electrode were characterized by scanning electron microscopy (SEM, Hitachi S-4800), X-ray diffraction (XRD, D/Max-III-type, Cu Ka X-ray source), and Raman (HORIBA Scientific LabRAM HR). The STXM analysis was performed at the Spectromicroscopy (SM) Beamline of the Canadian Light Source. Powder samples of LAGP-NCNT-Li_3InCl_6 before and after discharging were deposited on transmission electron microscopy (TEM) grids. Image
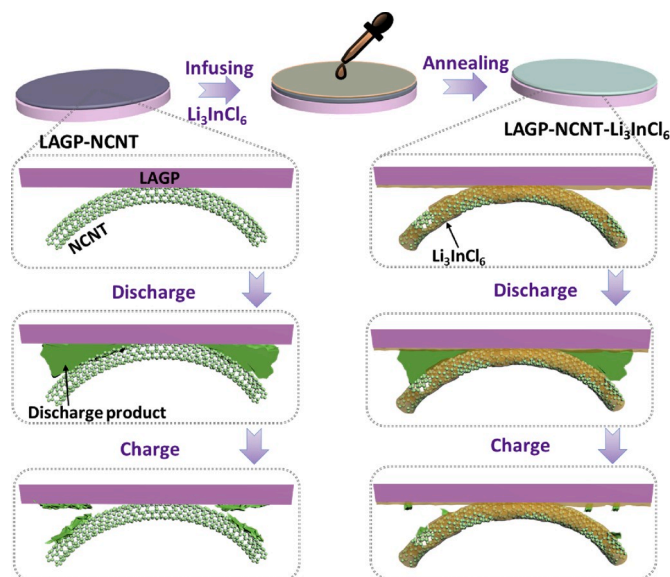
Scheme 1. Schematic illustration of the synthesis process for the LAGP-NCNT-Li_3InCl_6 air electrode and the effect of a Li_3InCl_6 modifier on the decomposition of discharge products.

stacks covering the C and O K-edges, and Cl L-edge were acquired on a single tube of sample. Elemental maps were derived by averaging the stack images of each element, and the spatially-resolved STXM-X-ray absorption near edge structure (XANES) spectra were selected from different regions on the sample.

Electrochemical Measurements: The electrochemical performance of SSLOBs was evaluated by building Swagelok-type cells in an Ar-filled glovebox with $O_2 < 0.1$ ppm and $H_2O < 0.1$ ppm. To prevent side reactions between the Li metal and LAGP pellet, a layer of thin GPE was used as an interlayer on the anode interface. The liquid electrolyte used in this work is 1 M LiClO$_4$ in TEGDME. The mass of liquid electrolyte used is equal to the mass of Li_3InCl_6 in the air electrode. The galvanostatic discharge-charge tests were conducted on an Arbin battery test system in 1 atm O_2 at room temperature. The current density and specific capacity are based on the mass of NCNT in the air electrode. The electrochemical impedance spectroscopy (EIS) and cyclic voltammetry (CV) tests were carried out on a Bio-Logic electrochemical workstation.

3. Results and discussion

Scheme 1 illustrates the synthesis process for the LAGP-NCNT-Li_3InCl_6 air electrode. The Li_3InCl_6 precursor solution was first dropped into the prepared LAGP-NCNT composite air electrode. After vacuum drying, the LAGP-NCNT-Li_3InCl_6 air electrode was obtained. The effect of the regulated ion channels on the decomposition of discharge products is also shown in Scheme 1.

The stability of Li_3InCl_6 toward both intermediate products and final products in Li–O_2 batteries has not been investigated before. In order to do this, a mixture of KO$_2$ powders and Li_3InCl_6 powders was fully ground and kept for 24 h. Fig. 1a shows that the XRD pattern of the mixture retains the diffraction patterns of the component compounds, indicating the stability of Li_3InCl_6 in the presence of KO$_2$. KO$_2$ is not an intermediate product in Li–O_2 batteries, it is just being used in lieu of LiO$_2$. Similarly, XRD patterns indicate no reaction between Li_2O_2 and Li_3InCl_6 (Fig. 1b). This is an important basic requirement for Li_3InCl_6 to be used in Li–O_2 batteries.

Fig. 1c–g shows the SEM images and energy-dispersive X-ray spectroscopy (EDX) results from the LAGP-NCNT-Li_3InCl_6 air electrode. As shown in Fig. S1, the pure LAGP-NCNT air electrode features a porous structure. NCNTs and LAGP particles are uniformly distributed and keep
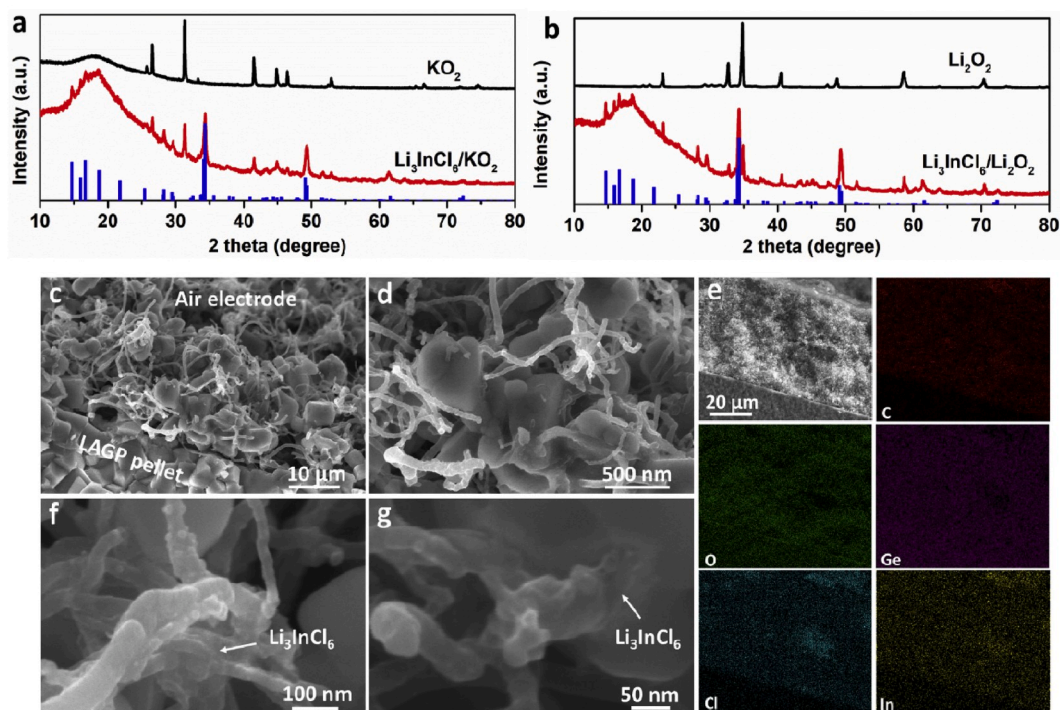
Fig. 1. XRD patterns of (a) KO_2 and the mixture of KO_2 and Li_3InCl_6, as well as (b) the Li_2O_2 and the mixture of Li_2O_2 and Li_3InCl_6. (c, d) SEM images of the LAGP-NCNT-Li_3InCl_6 air electrode. (e) SEM image and the corresponding EDX elemental mappings of C, O, Ge, Cl, and In. (f, g) Enlarged SEM images of the LAGP-NCNT-Li_3InCl_6 air electrode.
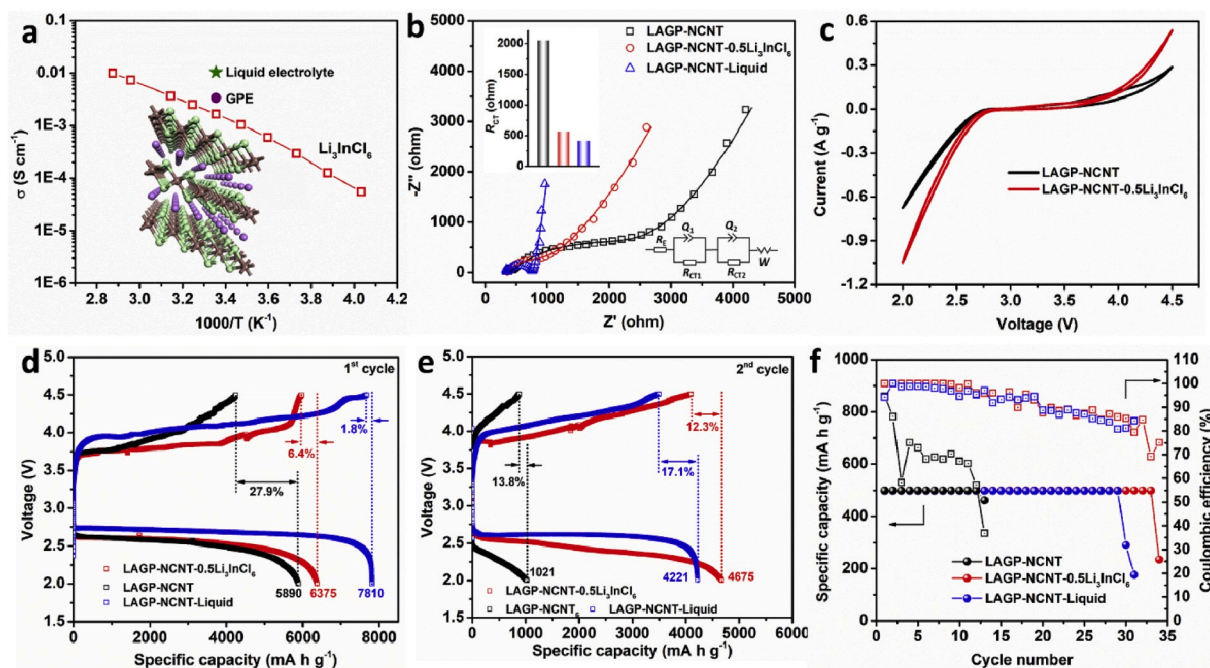

Fig. 2. (a) The ionic conductivity of Li_3InCl_6, GPE, and the LE, the inset is the crystal structure diagram of Li_3InCl_6. (b) Nyquist plots of the Li–O_2 batteries with LAGP-NCNT, LAGP-NCNT-0.5Li_3InCl_6, and LAGP-NCNT-Liquid air electrodes, respectively. (c) CV curves of the battery with LAGP-NCNT and LAGP-NCNT-0.5Li_3InCl_6 air electrodes, respectively. The (d) 1st cycle and (e) 2nd cycle discharge/charge profiles of the Li–O_2 battery with LAGP-NCNT, LAGP-NCNT-0.5Li_3InCl_6, and LAGP-NCNT-Liquid air electrodes, respectively, at a current density of 100 mA g^{-1}. (f) The cycling performance of Li–O_2 batteries with LAGP-NCNT, LAGP-NCNT-0.5Li_3InCl_6, and LAGP-NCNT-Liquid air electrodes, respectively.

intimate contact. As shown in Fig. 1c and d, after infusing Li_3InCl_6, the air electrode keeps its porous structure and maintains good contact with the LAGP pellet. The EDX elemental mappings show uniform

distribution of Cl and In consistent with the distribution of C, indicating that the Li_3InCl_6 was uniformly distributed throughout the air electrode (Fig. 1e). The Li_3InCl_6 was further observed with enlarged SEM images
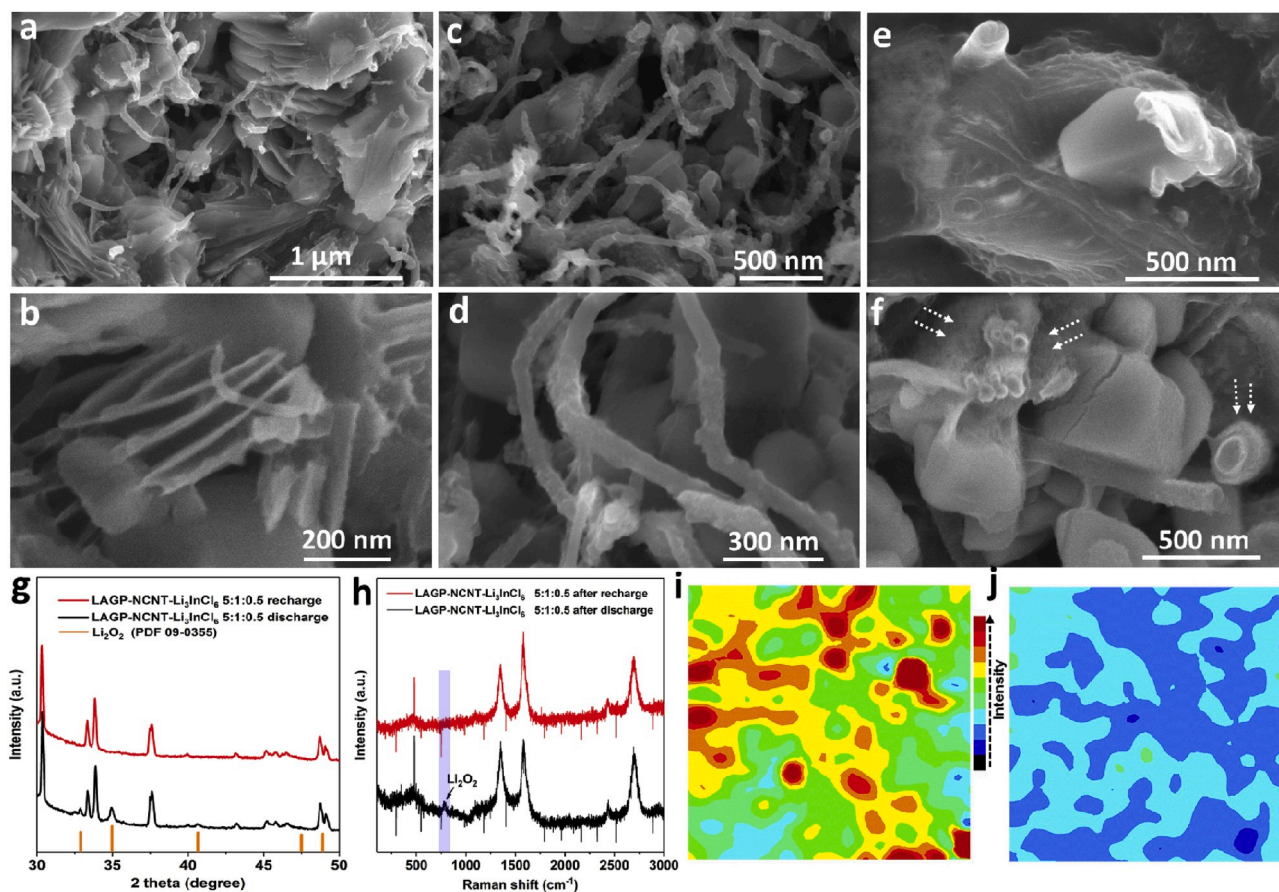
Fig. 3. SEM images of the LAGP-NCNT-0.5Li$_3$InCl$_6$ air electrode after (a, b) discharging and (c, d) recharging. SEM images of the LAGP-NCNT air electrode after (e) discharging and (f) recharging. (g) XRD patterns and (h) Raman spectra of the LAGP-NCNT-0.5Li$_3$InCl$_6$ air electrode after discharging and recharging. Raman mapping of the LAGP-NCNT-0.5Li$_3$InCl$_6$ air electrode after (i) discharging and (j) recharging.

(Fig. 1f and g). It is worth noting that the Li$_3$InCl$_6$ keeps intimate contact with the NCNT and LAGP. This regulates the ionic transport channels and increases the contacting surface area between ionic conductor and electronic conductor.

Next, the ionic conductivity of Li$_3$InCl$_6$ and its impact on the electrochemical performance of SSLOBs were investigated. As shown in Fig. 2a, the Li$_3$InCl$_6$ SSE exhibits an ultrahigh ionic conductivity of 1.3 × 10^{-3} S cm^{-1} at room temperature, which is comparable to the GPE and the LE in glass fiber separators. SSLOBs were tested by building Swagelok-type cells with LAGP-NCNT, LAGP-NCNT-0.5Li$_3$InCl$_6$, and LAGP-NCNT-Liquid air electrodes. In order to prevent side reactions between LAGP and Li metal and decrease the large interfacial resistance at the anode, a thin GPE with a thickness of 80 μm was used as an interlayer. Fig. 2b shows the EIS testing of the batteries. The Li$_3$InCl$_6$ modifier significantly decreases the interfacial resistance from 2056 Ω to 569 Ω, a value close to that of the battery with LE (414 Ω). As shown in Fig. 2c, the CV curve of the battery with Li$_3$InCl$_6$ exhibits higher ORR and OER peak currents than those of the original battery, indicating improved reaction kinetics.

Galvanostatic discharge-charge measurements were conducted at a current density of 100 mA g^{-1}. As shown in Fig. 2d, the battery with Li$_3$InCl$_6$ delivers an improved discharge capacity of 6375 mA h g^{-1} compared to that of the original battery (5890 mA h g^{-1}). More importantly, the Li$_3$InCl$_6$ modifier enhances the charge capacity of battery, indicating more effective decomposition of discharge products. The Coulombic efficiency is improved from 72.1% to 93.6% with Li$_3$InCl$_6$. As a result, the battery with Li$_3$InCl$_6$ delivers a discharge capacity of 4675 mA h g^{-1} in the 2nd cycle, which is much larger than that of the original battery (1021 mA h g^{-1}). Compared to the battery with

the LE, the battery with Li$_3$InCl$_6$ exhibits a decreased charge overpotential and a larger discharge capacity in the 2nd cycle.

In order to further investigate the effect of Li$_3$InCl$_6$ on the battery performance, air electrodes with different amounts of Li$_3$InCl$_6$ were prepared. Based on the mass ratio of Li$_3$InCl$_6$ to NCNT, the samples were labeled LAGP-NCNT-0.5Li$_3$InCl$_6$, LAGP-NCNT-1Li$_3$InCl$_6$, and LAGP-NCNT-2Li$_3$InCl$_6$. As shown in Fig. S2, the battery with the LAGP-NCNT-1Li$_3$InCl$_6$ air electrode exhibits an initial discharge capacity of 5160 mA h g^{-1} and a Coulombic efficiency of 99.1%. The discharge capacity in the 2nd cycle is 4680 mA h g^{-1}. The battery with the LAGP-NCNT-2Li$_3$InCl$_6$ air electrode delivers nearly 100% Coulombic efficiency in the 1st cycle despite a low discharge capacity (Fig. S3). The decreased capacity with increasing amounts of Li$_3$InCl$_6$ is due to the decreased electronic conductivity of the air electrode and decreased space for storing the discharge products.

Battery cycling performance was evaluated with a limited capacity of 500 mA h g^{-1} at a current density of 100 mA g^{-1}. As shown in Fig. 2f, the battery with Li$_3$InCl$_6$ exhibits significantly enhanced cycling performance from 12 cycles to 33 cycles. This cycling performance is superior to even that of the battery with the LE (29 cycles). Meanwhile, the battery with Li$_3$InCl$_6$ maintains an elevated Coulombic efficiency similar to that of the battery with LE (Fig. S4). In the 30th cycle, a Coulombic efficiency of 85.2% remains. In contrast, the Coulombic efficiency of the battery without the Li$_3$InCl$_6$ modifier decreases sharply during cycling. By the 10th cycle, the Coulombic efficiency has dropped to 67.1%. This indicates that the battery with LAGP-NCNT is unable to effectively decompose the discharge products. As a result, the undecomposed discharge products accumulate in the air electrode and result in polarization of the battery. When employing Li$_3$InCl$_6$ as a modifier, the
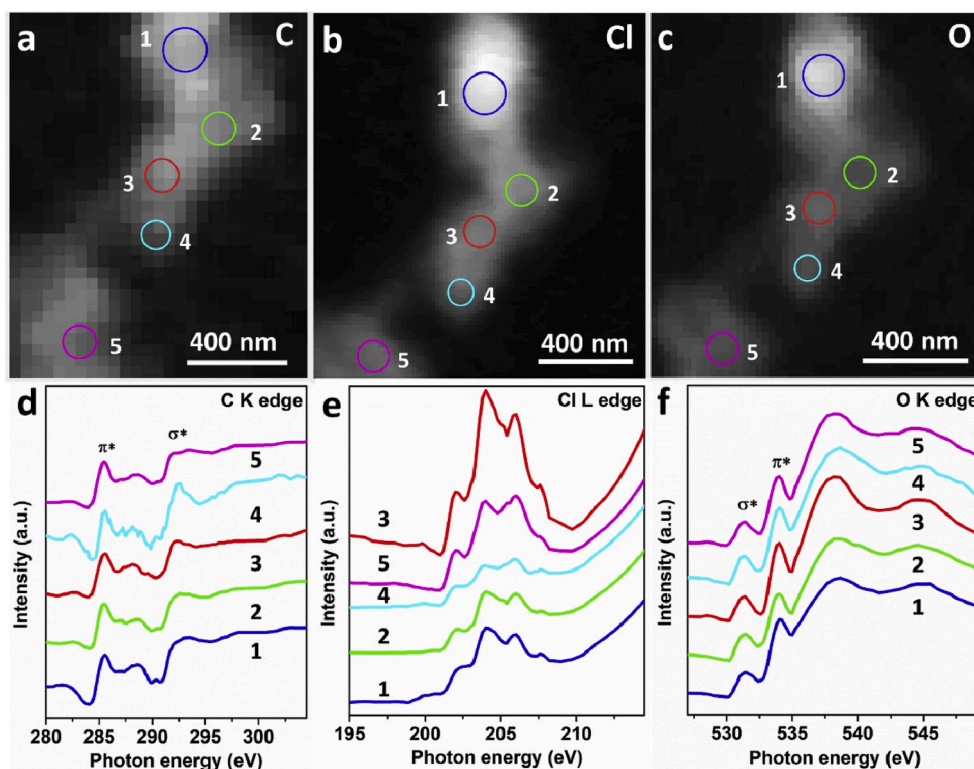
Fig. 4. STXM optical density images of (a) C, (b) Cl, and (c) O distributions in the discharged LAGP-NCNT-0.5Li$_3$InCl$_6$ and the corresponding XANES spectra of the (d) C K-edge, (e) Cl L-edge, and (f) O K-edge.

Li$_3$InCl$_6$ enhances the decomposition of discharge products and prolongs the cycle life. The Li$_3$InCl$_6$ plays a similar role to the LE by maintaining intimate contact between the NCNT and LAGP, thereby decreasing interfacial resistance. As shown in Scheme 1, the LAGP ionic conductor and NCNT electronic conductor in the LAGP-NCNT air electrode contact at a single point. Upon charging, if the discharge products become detached from either one, they will not be decomposed because of a lack of ion or electron transport. This explains the low Coulombic efficiency demonstrated by the LAGP-NCNT air electrode battery. When a small amount of LE is added into the LAGP-NCNT air electrode, the LE contacts the LAGP and NCNT and acts as ion channels. As a result, the battery with LE exhibits high Coulombic efficiency and enhanced cycling performance. Similarly, since Li$_3$InCl$_6$ is compatible with LAGP and NCNTs and has a high ionic conductivity, the Li$_3$InCl$_6$ modifier plays a role similar to that of a LE, regulating the interface between ionic conductor and electronic conductor and promoting the decomposition of discharge products. The relatively poor cycling stability of the battery with LE is due to the decomposition and evaporation of the finite volume of LE.

In order to further investigate the decomposition of discharge products in the presence of the Li$_3$InCl$_6$ modifier, the morphology of the air electrodes after discharging and recharging was investigated by SEM. Fig. 3a and b shows the SEM images of the LAGP-NCNT-0.5Li$_3$InCl$_6$ after discharging. The discharge products, featuring a nanosheet structure, deposit on the surface of air electrode. After recharging, discharge products are almost completely decomposed (Fig. 3c, d and S5). Fig. 3e shows an SEM image of the LAGP-NCNT after discharging. The discharge products are also deposited in the interface between LAGP and NCNT. In contrast to the LAGP-NCNT-0.5Li$_3$InCl$_6$ electrode, there remains some undecomposed discharge products in the LAGP-NCNT air electrode after recharging. These discharge products are detached from the NCNT and the LAGP (Fig. 3f). The ability for LAGP-NCNT-0.5Li$_3$InCl$_6$ to enhance discharge product decomposition was further confirmed by XRD and Raman tests. As shown in Fig. 3g, the XRD pattern of the discharged LAGP-NCNT-0.5Li$_3$InCl$_6$ air electrode shows

characteristic peaks of Li$_2$O$_2$ at 32.9°, 35.0°, and 40.7°. After recharging, these peaks disappear. However, this is not the case with a pure LAGP-NCNT air electrode (Fig. S6). These characteristic peaks are still present after recharging, indicating that the discharge products are not completely decomposed during charging. Fig. 3h shows a peak of 780 cm^{-1} in the Raman spectrum corresponding to Li$_2$O$_2$ in the LAGP-NCNT-0.5Li$_3$InCl$_6$ air electrode [42]. This peak disappears after recharging, consistent with the XRD and SEM results. To check the uniformity in distribution of discharge products and the effect of the LAGP-NCNT-0.5Li$_3$InCl$_6$ air electrode on the decomposition of discharge products, Raman mapping was conducted using the Li$_2$O$_2$ peak at 780 cm^{-1}. Fig. 3i shows a uniform, dense distribution of discharge products in the LAGP-NCNT-0.5Li$_3$InCl$_6$ after discharging. After recharging, the intensity of the Raman mapping decreases, suggesting the decomposition of discharge products (Fig. 3j).

In order to further confirm the good contact between NCNT and Li$_3$InCl$_6$, and the effect on regulating the interface, the discharged LAGP-NCNT-0.5Li$_3$InCl$_6$ air electrode was also investigated by STXM at the SM beamline of the Canadian Light Source. Fig. 4a–c shows STXM mappings of C, Cl, and O through averaging stack images at each elemental edge, which show similar shape and contrast, suggesting uniform distribution of these elements. The O mapping very closely resembles the Cl. The corresponding XANES spectra of C, Cl, and O are shown in Fig. 4d–f. The C K-edge spectra show typical NCNT features, including π*, σ* and the broad feature between 287 and 289 eV that involves π*C≡N and functionalization with discharged products. The O K-edge XANES spectra display an absorption feature at 531.5 eV which corresponds to the σ* (O–O) peak characteristic of Li$_2$O$_2$. The sharp absorption peak at 534 eV can be assigned to the transition to the π* (C═O) orbital in Li$_2$CO$_3$ [43]. The formation of Li$_2$CO$_3$ is posited to be due to the exposure to air during the preparation and test processes. The Cl L-edge XANES spectra maintain the same characteristics after discharging (Fig. S7), suggesting good stability during the electrochemical reaction. Based on these results, it is confirmed that the Li$_3$InCl$_6$ is stable toward Li$_2$O$_2$ and plays a

key role in regulating the deposition of Li_2O_2.

As discussed above, Li_3InCl_6 as a SSE is suitable for Li–O$_2$ batteries due to its good chemical stability and electrochemical stability. Li_3InCl_6 features a high ionic conductivity comparable to that of liquid electrolyte and can be prepared by a solution-based method. Batteries with Li_3InCl_6 show decreased interfacial resistance and exhibit enhanced decomposition of discharge products and longer cycle life, comparable to those of the battery with liquid electrolyte. Based on these merits, Li_3InCl_6 works like a liquid electrolyte modifier to regulate the air electrode interface.

4. Conclusion

In summary, we have developed a novel strategy to enhance the performance of SSLOBs by using a halide electrolyte as a modifier. Li_3InCl_6 features an ultrahigh ionic conductivity of 1.3×10^{-3} S cm^{-1} and can be uniformly infused into the air electrode through a solution method, leading to uniform distribution and intimate contact. As a result, this design decreases the interfacial resistance of SSLOBs and promotes the decomposition of discharge products. This work presents a comprehensive study on the use of Li_3InCl_6 in SSLOBs, which may shed light on a path to further research using halide electrolytes in SSLOBs.

Declaration of competing interest

The authors declare that they have no known competing financial interests or personal relationships that could have appeared to influence the work reported in this paper.

CRediT authorship contribution statement

Changtai Zhao: Conceptualization, Formal analysis, Investigation, Validation, Writing - original draft. **Jianwen Liang:** Methodology, Investigation. **Xiaona Li:** Methodology, Investigation. **Nathaniel Holmes:** Writing - review & editing. **Changhong Wang:** Methodology, Investigation. **Jian Wang:** Formal analysis. **Feipeng Zhao:** Formal analysis. **Shaofeng Li:** Formal analysis. **Qian Sun:** Formal analysis, Investigation. **Xiaofei Yang:** Formal analysis. **Jianneng Liang:** Formal analysis. **Xiaoting Lin:** Formal analysis. **Weihan Li:** Formal analysis. **Ruying Li:** Resources. **Shangqian Zhao:** Project administration, Funding acquisition. **Huan Huang:** Project administration, Funding acquisition. **Li Zhang:** Project administration, Funding acquisition. **Shigang Lu:** Project administration, Funding acquisition. **Xueliang Sun:** Conceptualization, Supervision.

Acknowledgements

Appendix A. Supplementary data

Supplementary data to this article can be found online at https://doi. org/10.1016/j.nanoen.2020.105036.

References

[1] A. Manthiram, X. Yu, S. Wang, Nat. Rev. Mater. 2 (2017) 16103.
[2] D. Lin, Y. Liu, Y. Cui, Nat. Nanotechnol. 12 (2017) 194.
[3] X.-B. Cheng, R. Zhang, C.-Z. Zhao, Q. Zhang, Chem. Rev. 117 (2017) 10403–10473.
[4] C. Yang, H. Xie, W. Ping, K. Fu, B. Liu, J. Rao, J. Dai, C. Wang, G. Pastel, L. Hu, Adv. Mater. 31 (2019) 1804815.
[5] C. Zhao, C. Yu, M.N. Banis, Q. Sun, M. Zhang, X. Li, Y. Liu, Y. Zhao, H. Huang, S. Li, X. Han, B. Xiao, Z. Song, R. Li, J. Qiu, X. Sun, Nano Energy 34 (2017) 399–407.
[6] J. Yi, H. Zhou, ChemSusChem 9 (2016) 2391–2396.
[7] J. Lu, L. Li, J.-B. Park, Y.-K. Sun, F. Wu, K. Amine, Chem. Rev. 114 (2014) 5611–5640.
[8] Q.-C. Liu, T. Liu, D.-P. Liu, Z.-J. Li, X.-B. Zhang, Y. Zhang, Adv. Mater. 28 (2016) 8413–8418.
[9] C. Zhao, C. Yu, S. Liu, J. Yang, X. Fan, H. Huang, J. Qiu, Adv. Funct. Mater. 25 (2015) 6913–6920.
[10] Y. Liu, J. Yi, Y. Qiao, D. Wang, P. He, Q. Li, S. Wu, H. Zhou, Energy Storage Mater. 11 (2018) 170–175.
[11] J. Yi, S. Guo, P. He, H. Zhou, Energy Environ. Sci. 10 (2017) 860–884.
[12] Y. Li, X. Wang, S. Dong, X. Chen, G. Cui, Adv. Energy Mater. 6 (2016) 1600751.
[13] X. Wang, D. Zhu, M. Song, S. Cai, L. Zhang, Y. Chen, ACS Appl. Mater. Interfaces 6 (2014) 11204–11210.
[14] Z. Zhang, Y. Shao, B. Lotsch, Y.-S. Hu, H. Li, J. Janek, L.F. Nazar, C.-W. Nan, J. Maier, M. Armand, L. Chen, Energy Environ. Sci. 11 (2018) 1945–1976.
[15] J. Sun, N. Zhao, Y. Li, X. Guo, X. Feng, X. Liu, Z. Liu, G. Cui, H. Zheng, L. Gu, H. Li, Sci. Rep. 7 (2017) 41217.
[16] X.B. Zhu, T.S. Zhao, Z.H. Wei, P. Tan, G. Zhao, Energy Environ. Sci. 8 (2015) 2782–2790.
[17] M. Balaish, E. Peled, D. Golodnitsky, Y. Ein-Eli, Angew. Chem. Int. Ed. 54 (2015) 436–440.
[18] Y. Zhu, X. He, Y. Mo, ACS Appl. Mater. Interfaces 7 (2015) 23685–23693.
[19] H. Muramatsu, A. Hayashi, T. Ohtomo, S. Hama, M. Tatsumisago, Solid State Ionics 182 (2011) 116–119.
[20] T. Ohtomo, A. Hayashi, M. Tatsumisago, K. Kawamoto, J. Mater. Sci. 48 (2013) 4137–4142.
[21] C. Zhao, J. Liang, Q. Sun, J. Luo, Y. Liu, X. Lin, Y. Zhao, H. Yadegari, M.N. Banis, R. Li, H. Huang, L. Zhang, R. Yang, S. Lu, X. Sun, Small Methods 3 (2019) 1800437.
[22] X. Zou, Q. Lu, Y. Zhong, K. Liao, W. Zhou, Z. Shao, Small 14 (2018) 1801798.
[23] N. Bonnet-Mercier, R.A. Wong, M.L. Thomas, A. Dutta, K. Yamanaka, C. Yogi, T. Ohta, H.R. Byon, Sci. Rep. 4 (2014) 7127.
[24] C. Zhao, J. Liang, Y. Zhao, J. Luo, Q. Sun, Y. Liu, X. Lin, X. Yang, H. Huang, L. Zhang, S. Zhao, S. Lu, X. Sun, J. Mater. Chem. A 7 (2019) 24947–24952.
[25] Z. Guo, C. Li, J. Liu, Y. Wang, Y. Xia, Angew. Chem. Int. Ed. 56 (2017) 7505–7509.
[26] H. Kitaura, H. Zhou, Sci. Rep. 5 (2015) 13271.
[27] Y. Liu, B. Li, Z. Cheng, C. Li, X. Zhang, S. Guo, P. He, H. Zhou, J. Power Sources 395 (2018) 439–443.
[28] X.B. Zhu, T.S. Zhao, Z.H. Wei, P. Tan, L. An, Energy Environ. Sci. 8 (2015) 3745–3754.
[29] W. Zhang, D.A. Weber, H. Weigand, T. Arlt, I. Manke, D. Schröder, R. Koerver, T. Leichtweiss, P. Hartmann, W.G. Zeier, J. Janek, ACS Appl. Mater. Interfaces 9 (2017) 17835–17845.
[30] M.D. Tikekar, S. Choudhury, Z. Tu, L.A. Archer, Nat. Energy 1 (2016) 16114.
[31] S. Xu, D.W. McOwen, C. Wang, L. Zhang, W. Luo, C. Chen, Y. Li, Y. Gong, J. Dai, Y. Kuang, C. Yang, T.R. Hamann, E.D. Wachsman, L. Hu, Nano Lett. 18 (2018) 3926–3933.
[32] X. Yu, A. Manthiram, Energy Environ. Sci. 11 (2018) 527–543.
[33] Y. Liu, P. He, H. Zhou, Adv. Energy Mater. 8 (2018) 1701602.
[34] X. Zhu, T. Zhao, P. Tan, Z. Wei, M. Wu, Nano Energy 26 (2016) 565–576.
[35] L. Xu, S. Tang, Y. Cheng, K. Wang, J. Liang, C. Liu, Y.-C. Cao, F. Wei, L. Mai, Joule 2 (2018) 1991–2015.
[36] L. Luo, B. Liu, S. Song, W. Xu, J.-G. Zhang, C. Wang, Nat. Nanotechnol. 12 (2017) 535.
[37] B. Wu, S. Wang, W.J. Evans Iv, D.Z. Deng, J. Yang, J. Xiao, J. Mater. Chem. A 4 (2016) 15266–15280.
[38] S. Wang, Q. Bai, A.M. Nolan, Y. Liu, S. Gong, Q. Sun, Y. Mo, Angew. Chem. Int. Ed. 58 (2019) 8039–8043.
[39] T. Asano, A. Sakai, S. Ouchi, M. Sakaida, A. Miyazaki, S. Hasegawa, Adv. Mater. 30 (2018) 1803075.
[40] X. Li, J. Liang, J. Luo, M. Norouzi Banis, C. Wang, W. Li, S. Deng, C. Yu, F. Zhao, Y. Hu, T.-K. Sham, L. Zhang, S. Zhao, S. Lu, H. Huang, R. Li, K.R. Adair, X. Sun, Energy Environ. Sci. 12 (2019) 2665–2671.
[41] X. Li, J. Liang, N. Chen, J. Luo, K.R. Adair, C. Wang, M.N. Banis, T.-K. Sham, L. Zhang, S. Zhao, S. Lu, H. Huang, R. Li, X. Sun, Angew. Chem. Int. Ed. 58 (2019) 16427–16432.
[42] D. Chalasani, B.L. Lucht, ECS Electrochem. Lett. 1 (2012) A38–A42.
[43] B.M. Gallant, D.G. Kwabi, R.R. Mitchell, J. Zhou, C.V. Thompson, Y. Shao-Horn, Energy Environ. Sci. 6 (2013) 2518–2528.